

Far Infrared Mapping of Three Galactic Star Forming Regions: W3(OH), S209 & S187

S. K. Ghosh^{1,2*}, B. Mookerjea^{1,3}, T. N. Rengarajan⁴, S. N. Tandon⁵ &
R. P. Verma¹

¹ Tata Institute of Fundamental Research, Bombay 400 005, India.

² Institute of Space and Astronautical Science, Kanagawa 229, Japan.

³ Joint Astronomy Programme, Indian Institute of Science, Bangalore 560 012, India.

⁴ Department of Physics, Nagoya University, Nagoya 464-8602, Japan.

⁵ Inter-University Centre for Astronomy & Astrophysics, Pune 411 007, India.

Received 2001 April 7; accepted 2001 May 20

Abstract. Three Galactic star forming regions associated with W3(OH), S209 and S187 have been simultaneously mapped in two trans-IRAS far infrared (FIR) bands centered at ~ 140 and $200\mu\text{m}$ using the TIFR 100 cm balloon borne FIR telescope. These maps show extended FIR emission with structures. The HIRES processed IRAS maps of these regions at 12, 25, 60 & $100\mu\text{m}$ have also been presented for comparison. Point-like sources have been extracted from the longest waveband TIFR maps and searched for associations in the other five bands. The diffuse emission from these regions have been quantified, which turns out to be a significant fraction of the total emission. The spatial distribution of cold dust ($T < 30\text{ K}$) for two of these sources (W3(OH) & S209), has been determined reliably from the maps in TIFR bands. The dust temperature and optical depth maps show complex morphology. In general the dust around S209 has been found to be warmer than that in W3(OH) region.

Key words. Interstellar dust—W3(OH)—S209—S187.

1. Introduction

The far infrared (FIR) continuum emission from the interstellar dust component allows one to probe deeper in to the denser regions of Galactic star forming regions. A long term programme of studying Galactic star forming regions is being pursued at the Tata Institute of Fundamental Research (TIFR) using its 100 cm balloon-borne FIR telescope. This programme aims at high resolution ($\sim 1'$) mapping in two FIR bands centered at wave-lengths ~ 150 and $200\mu\text{m}$, beyond the longest waveband of IRAS survey. The trans-IRAS wavebands help in detecting colder component of the dust. Several Galactic star forming regions have been studied leading to detection of cold dust (up to 15K) and its spatial distribution

*e-mail: swarna@tifr.res.in

(e.g. Ghosh *et al.* 2000; Mookerjea *et al.* 2000). The present study deals with three regions selected on the basis of their association with powerful molecular outflow activity and their extended/complex morphology. These are: W3(OH), S209 and S187 regions.

The Galactic star forming region known as W3(OH), is a very unique and interesting source for several reasons. It is situated $\sim 13'$ SE of W3 (main) in the giant molecular cloud, along the prominent ridge of star formation in the Perseus arm at a distance of 2.3 kpc. It is one of the most luminous high emission measure compact HII region of shell type morphology (Dreher & Welch 1981). Surrounding the ionized gas, there exist dense molecular clumps which host spectacular sources of OH, H₂O and CH₃OH maser emission as well as a bipolar outflow source (Wink *et al.* 1994). Tieftrunk *et al.* (1998) have surveyed this region in the NH₃ line in which they have detected extended emission. A strong far infrared source is associated with the HII region (Campbell *et al.* 1989). W3(OH) has received a lot of attention recently from cm, mm and sub-mm waveband researchers, though mostly concentrating on the higher spatial resolution of the very central few arc sec region. Here we present the study of the distribution of dust in the general neighbourhood of W3(OH) (within a few parsec).

The S209 region is an evolved HII region with visible optical nebulosity in the outer Galaxy. The ionized region is very extended and luminous in radio continuum. The emission at 1.4 GHz has been detected over $12' \times 7'$ by Fich (1993). The associated molecular gas extends over a region of $\sim 14'$ diameter, as inferred from the CO survey of Blitz, Fich & Stark (1982). The CO line velocity places S209 complex at a Galactocentric distance of 21 kpc, one of the outermost sites of star formation in the Galaxy (Fich & Blitz 1984). Molecular outflow activity has been inferred from broad CO wings by Wouterloot, Brand & Henkel (1988). A H₂O maser source has also been detected in the vicinity by Cesaroni *et al.* (1988). The above indicators confirm that star formation is still in progress in the S209 complex. Despite its large heliocentric distance (12 kpc), S209 is expected to be detectable in infrared wavebands due to its high intrinsic luminosity. Surprisingly, no study of the far infrared continuum emission from the S209 region exists in the literature.

S187 is an optical HII region (Sharpless 1959) located at the near side of dark cloud L1317 at a distance of 1 kpc, belonging to the Orion arm in the Galaxy. High angular resolution radio continuum map of this region shows the ionized gas to extend over $\sim 6'$ with rich structures (Snell & Bally 1986). Association of this region with a large molecular cloud complex has been known since Blair *et al.* (1975) detected extended CO emission from this region. Bally & Lada (1983) found first evidence for high velocity molecular outflow from S187, later confirmed to be of extended and bipolar nature by Casoli, Combes & Gerin (1984a). The full extent of this molecular complex has become more evident from the large scale surveys (though with crude gridding), carried out in ¹²CO and ¹³CO lines by Casoli, Combes & Gerin (1984b) and Yonekura *et al.* (1997). Various evidences of recent star formation activity in this region have been presented by Zavagno, Deharveng & Caplan (1994). The structurally rich emission from the molecular as well as the ionized gas, prompted us to study the emission from the dust component in S187.

The next two sections describe the observations and the results.

2. Observations

2.1 Balloon-borne observations

The Galactic star forming regions associated with W3(OH), S209 and S187 were mapped using the 12 channel two band far infrared (FIR) photometer system at the Cassegrain focus of the TIFR 100cm (f/8) balloon-borne telescope. The photometer uses a pair of six element (2×3 close packed configuration) composite Silicon bolometer arrays cooled to 0.3K using a closed cycle ^3He refrigerator and it has been described in Verma *et al.* (1993). The same region of the sky was viewed simultaneously in two FIR bands with near identical fields of view of $1.^{\circ}6$ per bolometer, thus instantaneously covering an area of $6.^{\circ}0 \times 3.^{\circ}4$ in each band. The sky was chopped along the cross-elevation axis at 10Hz with a throw of $4.^{\circ}2$. Full details of the 100cm telescope system and the observational procedure can be found in Ghosh *et al.* (1988). These sources were observed in two different balloon flights with slightly different FIR passbands of the photometer. The journal of observations and other details are presented in Table 1. The spectral responses of the two bands, relative responses of the detectors, absolute calibration of the photometer and other details specific to these two flights in 1993 and 1995 have been presented in Ghosh *et al.* (2000) and Mookerjea *et al.* (1999) respectively.

Table 1. The journal and other observational details.

Flight date	FIR target	λ_{eff} Ch-I (μm)	λ_{eff} Ch-II (μm)	Planet used	Planet FWHM Ch-I	Planet FWHM Ch-II
18th Nov 1993	W3(OH)	148	209	Jupiter	$1.^{\circ}0 \times 1.^{\circ}4$	$1.^{\circ}0 \times 1.^{\circ}3$
12th Nov 1995	S209 S187	138	205	Saturn	$1.^{\circ}6 \times 1.^{\circ}9$	$1.^{\circ}6 \times 1.^{\circ}8$

The observed chopped signals have been deconvolved using an indigenously developed procedure based on the Maximum Entropy Method (MEM) similar to that of Gull & Daniell (1978) (see Ghosh *et al.* 1988, for details). The accuracy of the absolute aspect of the telescope was improved by using a focal plane optical photometer which detects stars (in an offset field) while the telescope scans the FIR target source. The achieved absolute positional accuracy is $\sim 0.^{\circ}5$.

2.2 IRAS Data

The data from the IRAS survey in the four bands (12, 25, 60 and 100 μm) for the regions around the three target sources were HIRES processed (Aumann *et al.* 1990) at the Infrared Processing and Analysis Center (IPAC¹, Caltech). These maps have been used for extracting sources and quantifying interband positional associations and flux densities.

¹IPAC is funded by NASA as part of the IRAS extended mission program under contract to JPL.

3. Results

3.1 Intensity maps

The MEM deconvolved TIFR maps at 148 and 209 μm and the HIRES processed IRAS maps at 12, 25, 60 and 100 μm for the Galactic star forming region W3(OH) has been presented in Figs 1 and 2 respectively. Similarly, the intensity maps for S209 at 138, 205 μm and the IRAS bands have been presented in a similar format in Figs 3 and 4. Due to limited dynamic range achieved in the 138 μm band for S187, the intensity maps for this source are shown only at 205 μm and the IRAS bands (Figs 5 and 6).

Whereas the IRAS maps have very high dynamic ranges (>1000), the same for the TIFR maps is restricted to ~ 300 under the best circumstances. The contour levels displayed in TIFR maps for each programme source depend on the detector noise condition (which varied from time to time) at the time of the corresponding observations.

The angular resolution achieved in the TIFR bands is approximately represented by the deconvolved sizes of the point-like (planet) source in respective bands (see Table 1). All three programme sources, W3(OH), S209 and S187 show extended emission in both the TIFR bands.

The angular resolutions in the HIRES processed maps for each region are listed in Table 2, which depend on the observational details like relative orientation of scan tracks of the telescope boresight among different HCONs (Aumann, Fowler & Melnyk 1990). Although extensions are seen in many IRAS bands, the TIFR maps show superior angular resolution as a result of their smaller and circular beam.

Discrete sources have been extracted from the TIFR and HIRES maps using a procedure described in Ghosh *et al.* (2000). The longest wavelength channel (TIFR Ch-II) map has been used as the primary band. The sources detected in this are associated with sources in other bands if they satisfy the positional match criterion ($< 1'$ separation with TIFR Ch-I and $< 1.5'$ for HIRES bands). A total of nine sources in all three regions have been detected, details of which are listed in Table 3. Six of these have been detected in both the TIFR bands. All these nine sources have an association with

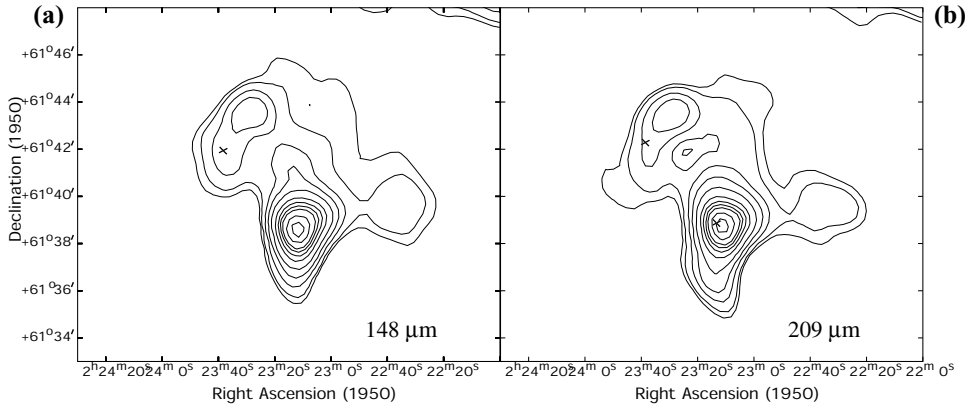


Figure 1. The intensity maps for the region around W3(OH) in TIFR bands :– (a) at 148 μm with peak = 3059 Jy/sq. arcmin, (b) at 209 μm with peak = 2101 Jy/sq. arcmin. The isophot contour levels in both (a) and (b) are 90, 70, 50, 40, 30, 20, 10, 5, 2.5, 1 & .5 % of the respective peaks. The crosses denote the positions of the IRAS PSC sources 02232 + 6138 (main source) & 02236 + 6142.

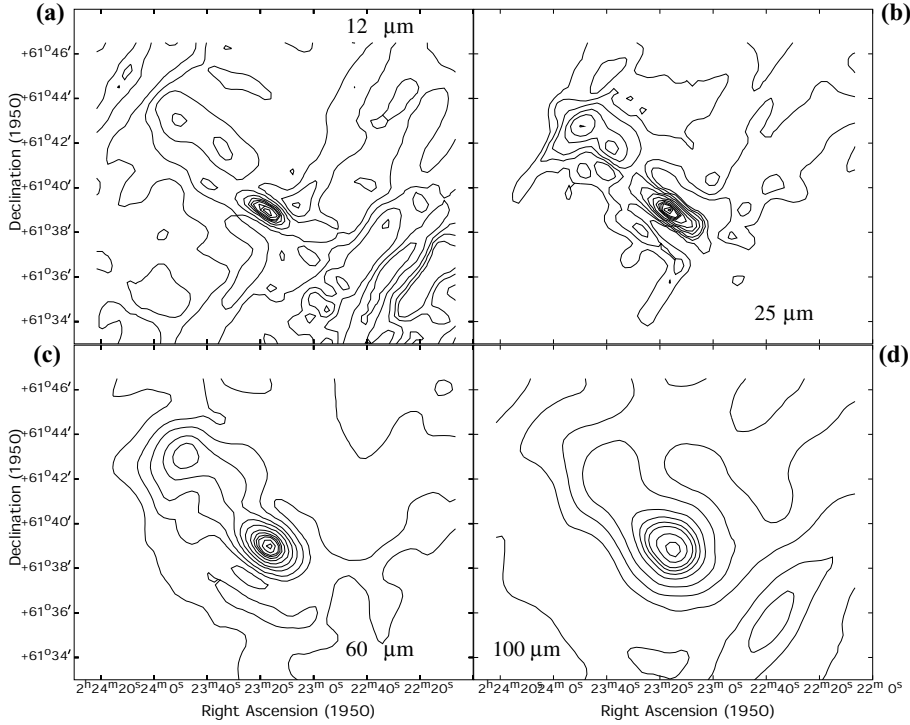


Figure 2. The HIRES processed IRAS maps for a similar region around W3(OH), as shown in Fig. 1, in the four bands :- (a) at $12 \mu\text{m}$ with peak = $66.9 \text{ Jy/sq. arcmin}$, (b) at $25 \mu\text{m}$ with peak = $1420 \text{ Jy/sq. arcmin}$, (c) at $60 \mu\text{m}$ with peak = $9870 \text{ Jy/sq. arcmin}$, (d) at $100 \mu\text{m}$ with peak = $3140 \text{ Jy/sq. arcmin}$. The isophot contour levels in (a) (b) & (c) are $90, 70, 50, 40, 30, 20, 10, 5, 2.5, 1, 0.5, \& 0.25\%$ of the respective peaks. In (d), only the higher 11 of these contours have been displayed.

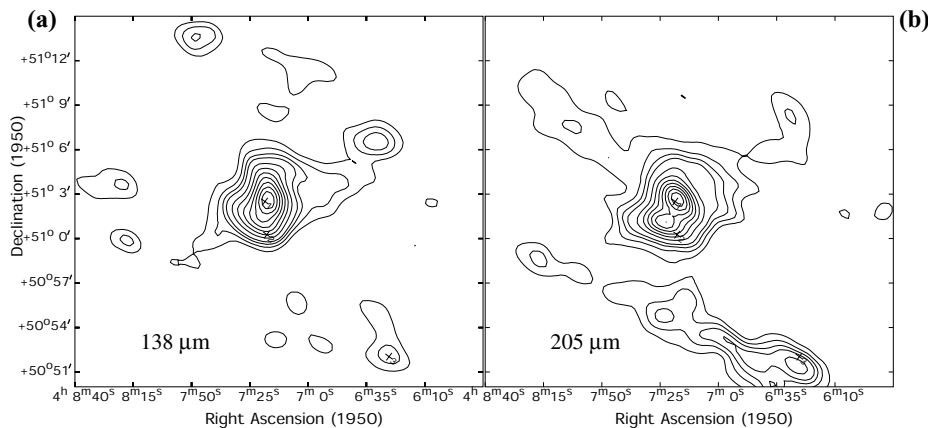


Figure 3. The intensity maps for the region around S209 in TIFR bands: (a) at $138 \mu\text{m}$ with peak = $441 \text{ Jy/sq. arcmin}$, (b) at $205 \mu\text{m}$ with peak = $213 \text{ Jy/sq. arcmin}$. The isophot contour levels in both (a) and (b) are $90, 80, 70, 60, 50, 40, 30, 20, 15, 10, \& 5\%$ of the respective peaks. The crosses denote the positions of the IRAS PSC sources $04073 + 5102$ (amin source), $04072 + 5100$ (the nearby source which is resolved in $205 \mu\text{m}$ map) and $04064 + 5052$.

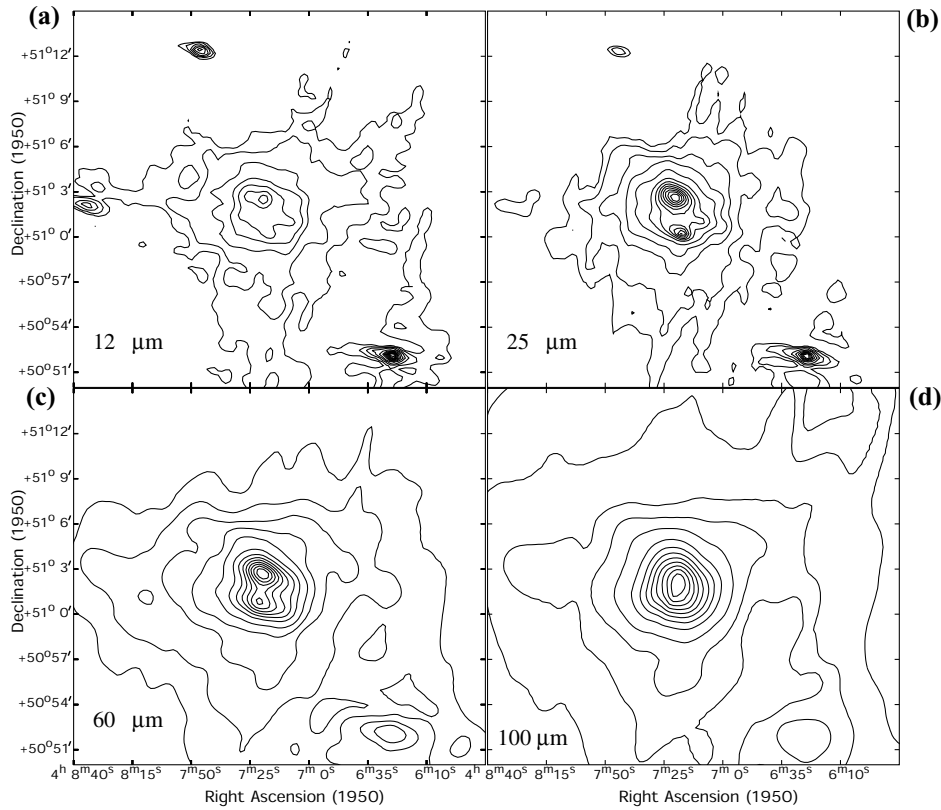


Figure 4. The HIRES processed IRAS maps for a similar region around S209, as shown in Fig. 3, in the four bands :- (a) at $12 \mu\text{m}$ with peak = $374 \text{ Jy/sq. arcmin}$, (b) at $25 \mu\text{m}$ with peak = $5470 \text{ Jy/sq. arcmin}$, (c) at $60 \mu\text{m}$ with peak = $12300 \text{ Jy/sq. arcmin}$, (d) at $100 \mu\text{m}$ with peak = $5830 \text{ Jy/sq. arcmin}$. The isophot contour levels in (a) are $30, 20, 10, 5, 2.5, 1 \& .5 \%$ of the peak, and in all the other three bands are $90, 80, 70, 60, 50, 40, 30, 20, 10, 5, 2.5, 1 \& .5 \%$ of the respective peaks.

HIRES source in at least one band (8 have associations in 2 or more IRAS bands). The listed flux densities have been obtained by integrating over a circle of $3'$ diameter. Six of these also appear in the IRAS Point Source Catalog (hereafter PSC). The PSC flux densities are also listed for comparison with those obtained from the HIRES maps. Four of these six PSC sources have upper limits in at least one IRAS band. This reflects the complexity of the morphology of these regions. The dust temperatures in the FIR, T_{FIR} , have been computed from the flux densities in the TIFR bands, assuming an emissivity law of $\epsilon_\lambda \propto \lambda^{-2}$. These are also listed in Table 3.

3.1.1 W3(OH)

Strong emission is seen in both 148 and $209 \mu\text{m}$ bands from W3(OH) and the peak position (S2) matches with that of the IRAS PSC source $02232 + 6138$ (Fig. 1). The corresponding source is also the strongest in all the four HIRES maps (Fig. 2). Whereas in TIFR bands S2 is resolved, it is pointlike in the IRAS bands. There are two other sources detected in both the TIFR maps. The second brightest source (S3)

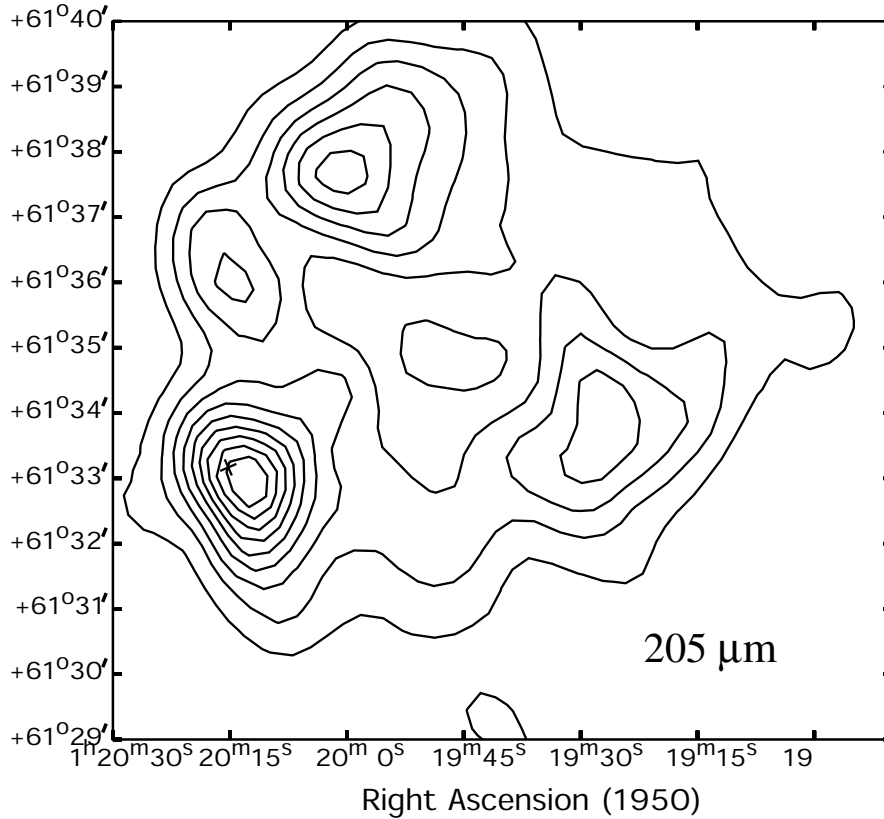


Figure 5. The intensity map for the region around S187 in TIFR band at $205\text{ }\mu\text{m}$. The isophot contour levels are 90, 80, 70, 60, 50, 40, 30, 20 & 10 % of the peak intensity (388 Jy/sq. arcmin). The cross denotes the position of the IRAS PSC source 01202 + 6133 (main source).

has counterparts in 12, 25 and 60 μm maps and a clear extension in 100 μm map. The diffuse emission has been detected in all the six bands.

The extension of the isophot contours towards NE of W3(OH) in the TIFR bands, match remarkably well with the plume ($\sim 2\text{pc} \times 1.3\text{pc}$) seen in the recent mapping in NH₃ line by Tieftrunk *et al.* (1998). In fact they concluded that the W3(OH) core is much larger than thought earlier.

Combining TIFR data along with the sub-millimeter measurement of Chini *et al.* (1986), the dust emissivity index is found to be 1.8 between 200 and 350 μm .

The total emission from a circular region of 16' diameter around the strong peak W3(OH), are 9601 and 6305 Jy at 148 and 209 μm respectively. The fraction of this in diffuse emission has been estimated to be 15% and 13% respectively by subtracting the contributions from the detected discrete sources (Table 3). A similar analysis of the IRAS-HIRES maps of the same region has quantified the diffuse emission to be 85, 55, 56 and 71% at 12, 25, 60 and 100 μm respectively. It may be noted that since the mapping in TIFR bands are carried out in sky chopped mode (in contrast to the IRAS bands), some part of the diffuse emission with low spatial gradient could have been missed in these bands. The total infrared luminosity estimated from the entire region is $1.91 \times 10^5 L_\odot$.

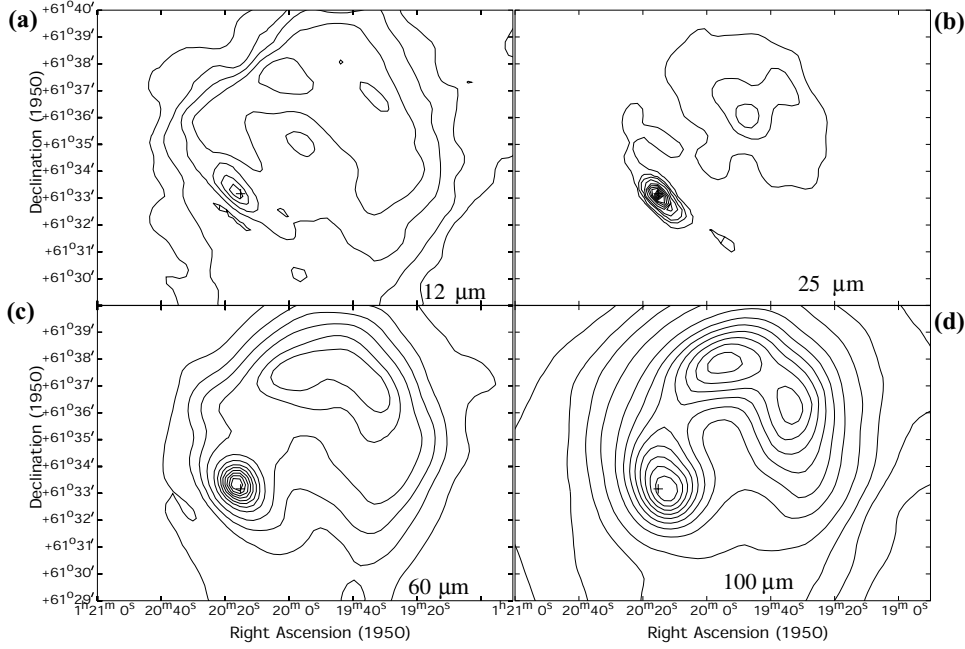


Figure 6. The HIRES processed IRAS maps for a similar region around S187, as shown in Fig. 5, in the four bands :- (a) at $12 \mu\text{m}$ with peak = $48.8 \text{ Jy/sq. arcmin}$, (b) at $25 \mu\text{m}$ with peak = $557 \text{ Jy/sq. arcmin}$, (c) at $60 \mu\text{m}$ with peak = $754 \text{ Jy/sq. arcmin}$, (d) at $100 \mu\text{m}$ with peak = $460 \text{ Jy/sq. arcmin}$. The isophot contour levels in (a) are 30, 20, 10, 5, 2.5 & 1% of the peak (the peak is outside the region displayed here) and in (b), (c) & (d) are 90, 80, 70, 60, 50, 40, 30, 20, 10, 5, 2.5, & 1% of the respective peaks.

Table 2. Angular resolutions in the HIRES maps.

Source region	Resolution at $12 \mu\text{m}$ FWHM	Resolution at $25 \mu\text{m}$ FWHM	Resolution at $60 \mu\text{m}$ FWHM	Resolution at $100 \mu\text{m}$ FWHM
W3(OH)	$74'' \times 29''$	$66'' \times 31''$	$114'' \times 57''$	$74'' \times 29''$
S209	$56'' \times 27''$	$54'' \times 28''$	$91'' \times 54''$	$110'' \times 64''$
S187	$39'' \times 27''$	$41'' \times 28''$	$76'' \times 46''$	$113'' \times 97''$

3.1.2 S209

There is a good correlation and structural similarity between the extended emission from the dust component in all the six bands. The complex emission structure has restricted the reliable source extraction for the IRAS Point Source Catalog as evident from inconsistent flux densities in different bands for the main source corresponding to S209, IRAS 04073 + 5102. However, numerical aperture photometry on HIRES processed IRAS maps provide reliable estimates of flux densities.

The main source in the S209 region is clearly resolved into two sources (S5 & S6) at $205 \mu\text{m}$ map and there is indication for the same in the $138 \mu\text{m}$ map (Fig. 3).

Table 3. Position and flux density details of the detected sources.

#	RA (1950) h m s	Dec (1950) o ' ''	IRAS PSC associations	Flux Density (Jy)					T_{FIR}^b (K)	
				TIFR		IRAS ^a				
				209 / 205 μm	148 / 138 μm	100 μm	60 μm	25 μm	12 μm	
W3(OH) Region										
S1	2 22 28.3	+61 39 32	...	128	260	–	–	35	30	30
S2	2 23 11.3	+61 38 54	02232+6138	4872	7198	10030	9488	683	66	22
	"	"	"			10600 ^c	9269 ^c	535 ^c	40.6 ^c	
S3	2 23 29.0	+61 43 34	02236+6142	476	744	1886	901	67	36	23
	"	"	"			<10600 ^c	<1712 ^c	<91 ^c	12.3 ^c	
S209 Region										
S4	4 06 26.7	+50 51 18	04064+5052	323	224	190	149	48	30	15
	"	"	"			171.2 ^c	83.4 ^c	43.3 ^c	25.4 ^c	
S5	4 07 17.4	+51 02 45	04073+5102	970	2139	2298	2159	409	70	31
	"	"	"			2723 ^c	<0.4 ^c	97 ^c	16 ^c	
S6	4 07 22.6	+51 01 07	04072+5100	873	–	–	1905	236	38	–
	"	"	"			<2700 ^c	<439 ^c	41 ^c	2.4 ^c	
S187 Region										
S7	1 19 25.7	+61 34 02	...	885	1770	–	829	–	41	28
S8	1 20 01.3	+61 37 45	...	1094	–	2005	1310	–	52	–
S9	1 20 13.6	+61 32 52	01202+6133	1304	–	1908	1400	211	32	–
	"	"	"			<1700 ^c	882 ^c	182 ^c	10.4 ^c	

^a From HIRES processed maps unless specified otherwise. The flux densities are integrated over a circle of 3.'0 diameter.^b Determined using the flux densities in TIFR bands and assuming a gray body spectrum with emissivity $\epsilon_\lambda \propto \lambda^{-2}$.^c From IRAS Point Source Catalog.

The strongest peaks in both the TIFR bands (S5) coincide with the position of IRAS 04073 + 5102. The neighbouring source S6 is associated with IRAS 04072 + 5100. In 25 and 60 μm IRAS bands, S6 is clearly seen and an indication is present in the 12 μm map (Fig. 4). The 100 μm HIRES processed map does not resolve S5/S6.

Chini *et al.* (1984) have detected S209 in 1-mm continuum and presented the thermal emission from the dust after correcting for the expected free free emission from the hot gas. Using the flux densities at 205 μm and 1-mm, a very flat dust emissivity exponent of 0.64 has been found for this sub-mm region. In case the emission at 1-mm originates from a different colder dust component, then the above index is an underestimate.

The total emission from the S209 region presented in Fig. 3 is 5548 and 4000 Jy at 138 and 205 μm respectively. The fraction of this in diffuse emission has been estimated to be 57% and 46% respectively by subtracting the contributions from the detected discrete sources. A similar analysis of the IRAS-HIRES maps of the same region (Fig. 4) has quantified the diffuse emission to be 52, 44, 49 and 77% at 12, 25, 60 and 100 μm respectively. Hence right through the mid and far infrared region, a good part of the emission is in diffuse form. The total infrared luminosity estimated from the entire region is $2.0 \times 10^6 L_\odot$ (for distance = 12 kpc).

Balser *et al.* (1995) have modelled their 8.7 GHz radio continuum measurements of the S209 region ($8' \times 8'$) and they conclude that the exciting source is either a ZAMS O6.5 star or a O5 star depending on the data used (VLA / MPIR). These stellar types correspond to a luminosity of $1.5 \times 10^5 L_\odot$ or $6.8 \times 10^5 L_\odot$ respectively (Thompson 1984).

3.1.3 S187

The dynamic range of the TIFR maps of S187 region is rather limited due to larger than usual noise in the bolometer channels during these observations (only the 205 μm map presented here). The strongest source (S9) associated with IRAS 01202 + 6133 is resolved at 205 μm (Fig. 5). The morphology of the diffuse emission in the TIFR band resembles the same in the HIRES maps (Fig. 6). This is despite the fact that TIFR observations used sky chopping whereas IRAS survey did not. The emissions in all the five bands are dominated by the source associated with IRAS 01202 + 6133. Most of the additional emission originates from an annular ring like structure of diameter $\sim 10'$. The ionized gas resides at the central cavity of the annular region as inferred from high resolution radio continuum map at 1.4 GHz (Snell & Bally 1986). The position of the high velocity molecular outflow lies about 2' west of S9. The H₂O maser source detected by Henkel, Haschick & Gusten (1986) is positionally very close to the outflow source. No local enhancement has been observed in any of the TIFR or HIRES bands at the location of the H₂O maser/outflow source. The position of the NH₃ core detected in the S187 region (Jijina, Myers & Adams 1999), also does not show positional match with any peak in the maps of dust continuum emission.

The total emission from the S187 region presented in Fig. 5 is 7256 Jy at 205 μm . The fraction of this in diffuse emission has been estimated to be 55% by subtracting the contributions from the detected discrete sources. A similar analysis of the IRAS-HIRES maps of the same region (Fig. 6) has quantified the diffuse emission to be 66, 68, 53 and 69% at 12, 25, 60 and 100 μm respectively. For this source too, right through the mid and far infrared region, a large part of the emission is in diffuse form, which is

quite expected considering the complex morphology of the region. The total infrared luminosity estimated from the entire region is $1.7 \times 10^4 L_\odot$ (for distance = 1 kpc).

Using the mass of the molecular cloud associated with S187, as estimated by Yonekura *et al.* (1997) from their ^{13}CO survey (their cloud # 164), we determine the average luminosity per unit mass to be $\sim 2.2 L_\odot/M_\odot$. This value is very similar to that found for W 31 star forming complex (Ghosh *et al.* 1989).

3.2 Distribution of dust temperature and optical depth

Taking advantage of the nearly identical circular beams of the TIFR bands and the simultaneity of observations, reliable maps of dust temperature and optical depth (at 200 μm , τ_{200}) have been generated for W3(OH) and S209 regions. The available dynamic ranges in both the TIFR bands for these two sources allow us to meaningfully determine the dust temperature and optical depth distributions. These are presented in Figs. 7 and 8 respectively. A dust emissivity law of $\epsilon_\lambda \propto \lambda^{-2}$ has been assumed for this purpose. Details of the procedure can be found in Ghosh *et al.* (2000).

For W3(OH) region, the distribution of τ_{200} shows a peak near the intensity peak but the $T(148/209)$ distribution shows a plateau there (Fig. 7). Some regions of higher dust temperature are also seen. The second peak in the optical depth map clearly corresponds to the matter distribution around 02236 + 6142. The dust temperature at the position of IRAS 02232 + 6138 is 21K, whereas the kinetic temperature of the NH_3 component has been found to be 27K (Tieftrunk *et al.* 1998). In addition, the shape of the τ_{200} distribution around IRAS 02232 + 6138 (within 2') resembles the gas distribution traced by NH_3 . A detailed comparison should help understanding the gas-dust coupling in denser regions of star formation, like the interstellar environment around W3(OH).

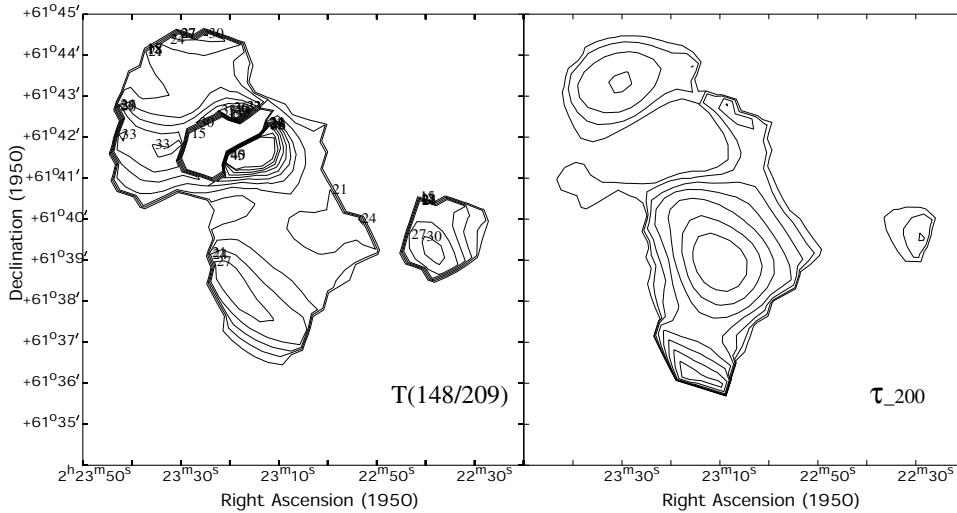


Figure 7. The distribution of dust temperature $T(148/209)$, and optical depth at 200 μm , τ_{200} , for the region around W3(OH) assuming a dust emissivity law of $\epsilon_\lambda \propto \lambda^{-2}$. The isotherms correspond to 15K to 36K in steps of 3K, 40 & 45K. Temperature values are displayed near the contours. The highest contour of τ_{200} (innermost at the bottom) corresponds to a value of 0.16 and the successive contours represent values reducing by factor of 2.

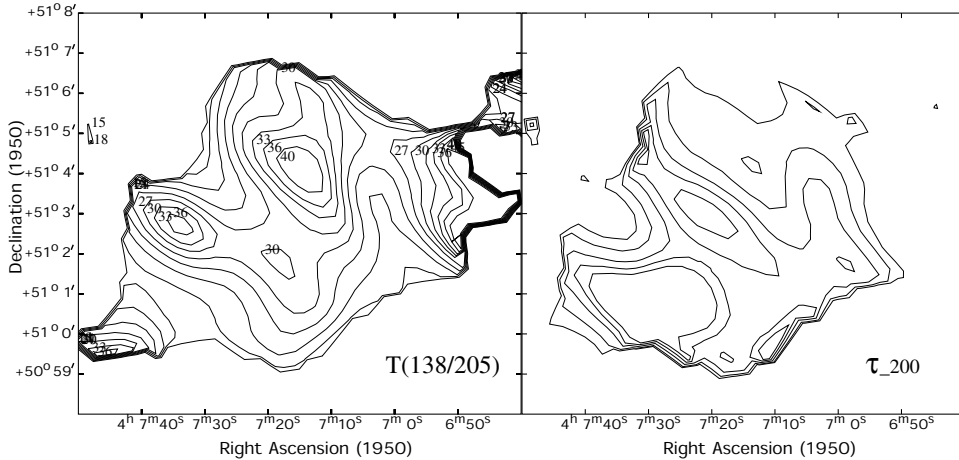


Figure 8. The distribution of dust temperature $T(138/205)$, and optical depth at $200\mu\text{m}$, τ_{200} , for the region around S209 assuming a dust emissivity law of $\epsilon_\lambda \propto \lambda^{-2}$. The isotherms refer to the same temperatures as in Fig. 7. The τ_{200} contours represent 100, 75, 50, 25 & 12.5 % of the peak value of 0.67.

The $T(138/205)$ and τ_{200} distributions for S209 show an almost anticorrelation (Fig. 8). The hotspots are located near the two resolved sources in the $205\mu\text{m}$ map. Most of the region in S209 has the dust temperature higher than 27 K and the presence of colder dust is limited to the outermost periphery. This is in contrast to W3(OH) region where the dust is relatively cooler.

Acknowledgements

We thank S. L. D’Costa, M. V. Naik, S. V. Gollapudi, D. M. Patkar, M. B. Naik and G. S. Meshram for their support for the experiment. The members of TIFR Balloon Facility (Balloon group and Control & Instrumentation group), Hyderabad, are thanked for their roles in conducting the balloon flights. IPAC is thanked for providing HIRES processed IRAS data. SKG thanks the Institute of Space and Astronautical Science (ISAS), Japan, for their hospitality, where part of the work was done.

References

- Aumann, H. H., Fowler, J. W., Melnyk, M. 1990, *Astr. J.* **99**, 1674.
- Bally, J., Lada, C. J. 1983, *Astrophys. J.* **265**, 824.
- Balser, D. S., Bania, T. M., Rood, R. T., Wilson, T. L. 1995, *Astrophys. J. Suppl.* **100**, 371.
- Blair, G. N., Peters, W. L., van den Bout, P. A. 1975, *Astrophys. J.* **200**, L161.
- Blitz, L., Fich, M., Stark, A. A. 1982, *Astrophys. J. Suppl.* **49**, 183.
- Campbell, M. F., Lester, D. F., Harvey, P. M., Joy, M. 1989, *Astrophys. J.* **345**, 298.
- Casoli, F., Combes, F., Gerin, M. 1984a, *Astr. Astrophys.* **133**, 99.
- Casoli, F., Combes, F., Gerin, M. 1984b, *Nearby molecular clouds*, G. Serra (ed.), Lecture Notes in Physics no. 237, p. 136, (Berlin-Heidelberg: Springer-Verlag).
- Cesaroni, R. et al. 1988, *Astr. Astrophys. Suppl.* **76**, 445.
- Chini, R., Krugel, E., Kreysa, E. 1986, *Astr. Astrophys.* **167**, 315.
- Chini, R., Mezger, P. G., Kreysa, E., Gemund, H. P. 1984, *Astr. Astrophys.* **135**, L14.

- Dreher, J. W, Welch, W. J. 1981, *Astrophys. J.* **245**, 857.
Fich, M. 1993, *Astrophys. J. Suppl.* **86**, 475.
Fich, M., Blitz, L. 1984, *Astrophys. J.* **279**, 125.
Ghosh, S. K., Iyengar, K. V. K., Rengarajan, T. N., Tandon, S. N., Verma, R. P., Daniel, R. R. 1988, *Astrophys. J.* **330**, 928.
Ghosh, S. K., Iyengar, K. V. K., Rengarajan, T. N., Tandon, S. N., Verma, R. P., Daniel, R. R., Ho P. T. P. 1989, *Astrophys. J.* **347**, 338.
Ghosh, S. K., Mookerjea, B., Rengarajan, T. N., Tandon, S. N., Verma, R. P. 2000, *Astr. Astrophys.* **363**, 744.
Gull, S. F., Daniell, G. J. 1978, *Nature* **272**, 686.
Henkel, C., Haschick, A. D., Gusten, R., 1986, *Astr. Astrophys.* **165**, 197.
Jijina, J., Myers, P. C., Adams, F. C. 1999, *Astrophys. J. Suppl.* **125**, 161.
Mookerjea, B., Ghosh, S. K., Karnik, A. D., Rengarajan, T. N., Tandon, S. N., Verma R. P. 1999, *Astrophys. J.* **522**, 285.
Mookerjea, B., Ghosh, S. K., Rengarajan, T. N., Tandon, S. N., Verma, R. P. 2000, *Astr. J.* **120**, 1954.
Sharpless, S. 1959, *Astrophys. J. Suppl.* **4**, 257.
Snell, R. L., Bally, J. 1986, *Astrophys. J.* **303**, 683.
Thompson, R. I. 1984, *Astrophys. J.* **283**, 165.
Tieftrunk, A. R., Megeath, S. T., Wilson, T. L., Rayner, J. T. 1998, *Astr. Astrophys.* **336**, 991.
Verma, R. P., Rengarajan, T. N., Ghosh, S. K. 1993, *Bull. Astron. Soc. India* **21**, 489.
Wink, J. E., et al 1994, *Astr. Astrophys.* **281**, 505.
Wouterloot, J. G. A., Brand, J., Henkel, C. 1988, *Astr. Astrophys.* **191**, 323.
Yonekura, Y., Dobashi, K., Mizuno, A., Ogawa, H., Fukui, Y. 1997, *Astrophys. J. Suppl.* **110**, 21.
Zavagno, A., Deharveng, L., Caplan, J. 1994, *Astr. Astrophys.* **281**, 491.